INTERNATIONAL JOURNAL FOR NUMERICAL METHODS IN FLUIDS
Int. J. Numer. Meth. Fluids 2009; **61**:355–381
Published online 2 December 2008 in Wiley InterScience (www.interscience.wiley.com). DOI: 10.1002/fld.1960

Optimal airfoil shapes for low Reynolds number flows

D. N. Srinath and S. Mittal*, †

Department of Aerospace Engineering, Indian Institute of Technology Kanpur, Kanpur, UP 208 016, India

SUMMARY

Flow over NACA 0012 airfoil is studied at $\alpha = 4°$ and 12° for $Re \leqslant 500$. It is seen that the flow is very sensitive to *Re*. A continuous adjoint based method is formulated and implemented for the design of airfoils at low Reynolds numbers. The airfoil shape is parametrized with a non-uniform rational B-splines (NURBS). Optimization studies are carried out using different objective functions namely: (1) minimize drag, (2) maximize lift, (3) maximize lift to drag ratio, (4) minimize drag and maximize lift and (5) minimize drag at constant lift. The effect of Reynolds number and definition of the objective function on the optimization process is investigated. Very interesting shapes are discovered at low *Re*. It is found that, for the range of *Re* studied, none of the objective functions considered show a clear preference with respect to the maximum lift that can be achieved. The five objective functions result in fairly diverse geometries. With the addition of an inverse constraint on the volume of the airfoil the range of optimal shapes, produced by different objective functions, is smaller. The non-monotonic behavior of the objective functions with respect to the design variables is demonstrated. The effect of the number of design parameters on the optimal shapes is studied. As expected, richer design space leads to geometries with better aerodynamic properties. This study demonstrates the need to consider several objective functions to achieve an optimal design when an algorithm that seeks local optima is used. Copyright © 2008 John Wiley & Sons, Ltd.

Received 22 April 2008; Revised 2 October 2008; Accepted 2 October 2008

KEY WORDS: airfoils; objective functions; shape optimization; adjoint methods; finite element; fluid flow; low Reynolds numbers

1. INTRODUCTION

Aerodynamic shape optimization is being increasingly accepted as a design tool. With increasing computing abilities and better algorithms and strategies more complex design problems are being undertaken. Several techniques have been tried for carrying out aerodynamic shape optimization. Some of the methods are random search methods [1], complex Taylor series expansion approach [2], automatic differentiation method [3], direct differentiation method [4] and adjoint

*Correspondence to: S. Mittal, Department of Aerospace Engineering, Indian Institute of Technology Kanpur, Kanpur, UP 208 016, India.
†E-mail: smittal@iitk.ac.in

based methods [5]. Among the most commonly used methods are gradient based methods in which a specified objective function is minimized or maximized with respect to design shape parameters. Of particular interest are adjoint based methods. In these methods the flow equations are adjoined or augmented to the objective function by the use of Lagrange multipliers. Adjoint based methods provide a economical framework to work with a large number of design variables. Pioneering work in these methods can be found in [6–8].

The adjoint based methods can be classified as continuous *vs* discrete. In the continuous adjoint method, first the variation of the augmented objective function is derived. The resulting equations are then discretized. In the discrete adjoint methods the discretization process precedes the variation. Comparison of the two approaches can be found in [9, 10]. It is seen that as the grid spacing approaches zero, both methods yield same results. The advantage of the continuous adjoint method is that once the variation of the equations is found, the same can be utilized for any discretization.

Design methods can be one of the two types: inverse or direct. In an inverse design method the aerodynamic characteristics are predefined. An example of the inverse problem is the design of an airfoil shape that results in a certain prescribed pressure distribution. Direct design methods, on the contrary, attempt to seek a local optima in the design space. An example of the direct problem is one in which one seeks to find the shape that has the least drag. The possibility of the optimum being the global optimum depends on the choice of the initial guess in the optimization process. Multiple local optima can be found by changing the initial guess [11].

Significant research is being carried out in the design of small sized flying vehicles, namely, micro aerial vehicles [12]. Flow around micro structures are also beginning to form an integral part of many applications of micro electromechanical systems(MEMS) [13]. Power MEMS [14] is a rapidly growing field describing microsystems which generate power or pumped heat. Another area generating lot of interest is the design of micro flying robots [15]. Despite significant interest in applications at small scales not much data exists, either experimental or numerical, at extremely low *Re*.

Significant research has been carried out for airfoils at high *Re* [16, 17] including optimization studies [18, 19]. It is well known that airfoils designed for high Reynolds number operation are not optimal at low *Re*. A good source of airfoil data at low *Re* is Carmichael [20]. Thom and Swart [21] carried out experiments with a R.A.F. 6a airfoil at *Re* as low as 0.5. Sunada *et al.* [22] studied the aerodynamic characteristics of various airfoils at $Re=4000$, by varying parameters such as thickness, camber and roughness. They found that, at low *Re*, thinner airfoils have better aerodynamic characteristics. Sun and Boyd [23] used a hybrid continuum-particle approach to compute flow over a 5% thick flat plate at Reynolds number varying between 1 and 200. They noticed that the lift to drag ratio drops below unity for Reynolds numbers less than 50. They also notice that the drag coefficient increases with decrease in *Re*. Kunz [24] observed that the maximum lift coefficient of airfoils increases with decreasing *Re*. At very low Reynolds numbers not only are the optimal airfoils thinner, but the camber also plays a major role. Yagi and Kawahara [25] carried out drag minimization at $Re=250$. Starting from a circular cylinder their design cycle led to an airfoil shape. However, they observed that the shape with minimum drag has a sharp leading edge and a rounded trailing edge, much like a conventional airfoil placed at 180° angle of attack.

There are two main objectives of this study. Firstly, to evaluate the relative performance of various objective functions to design an optimal airfoil. The second objective is to investigate the variation in optimal airfoil geometries with *Re* in the steady laminar flow regime. Flow over NACA 0012 airfoil is studied at $\alpha=4°$ and 12° at $Re\leqslant 500$. Optimization studies are then carried out to determine the best shapes for $\alpha=4°$ and 12°. Five different direct objective functions are

DOI: 10.1002/fld

considered. They are (1) to minimize drag, (2) to maximize lift, (3) to maximize the lift to drag ratio, (4) to maximize lift and minimize drag and (5) to minimize drag at constant lift. A geometric constraint, namely the preservation of volume is further imposed and the study is repeated. An unstructured grid is used to accommodate the possible change in airfoil shapes. A mesh moving scheme [26] is employed to generate grids for updated geometries.

In the present work, a continuous adjoint based method in the context of steady, incompressible low Reynolds number flows is implemented for airfoil design. A stabilized finite element method based on the streamline-upwind Petrov/Galerkin (SUPG) and pressure-stabilizing Petrov/Galerkin (PSPG) [27] stabilization techniques is employed to solve, both, the flow and the adjoint equations. The limited memory-Broyden-Fletcher-Goldfarb-Shanno (L-BFGS) algorithm [28] is used to minimize the objective function. The airfoil shape is parametrized by a 4th order non-uniform rational B-splines curve(NURBS) [29].

2. GOVERNING EQUATIONS

2.1. Flow equations

Consider a domain Ω, with boundary Γ, that is occupied by a fluid of density ρ and dynamic viscosity μ. The governing equations for a steady incompressible flow of this fluid are given as:

$$\rho\mathbf{u}.\nabla\mathbf{u}+\nabla.\boldsymbol{\sigma}=\mathbf{f} \quad \text{on } \Omega \tag{1}$$

$$\nabla.\mathbf{u}=0 \quad \text{on } \Omega \tag{2}$$

where $\mathbf{u}$ is the velocity, $\boldsymbol{\sigma}$ the stress tensor and $\mathbf{f}$ the body force. For a Newtonian fluid the stress tensor is given as $\boldsymbol{\sigma}=-p\mathbf{I}+\mu[\nabla\mathbf{u}+(\nabla\mathbf{u})^{\mathrm{T}}]$ where, p is the pressure and $\mathbf{I}$ the identity tensor. The boundary conditions are either on the flow velocity or stress. Both, Dirichlet and Neumann type boundary conditions are accounted for:

$$\mathbf{u}=\mathbf{g} \quad \text{on } \Gamma_g \tag{3}$$

$$\mathbf{n}.\boldsymbol{\sigma}=\mathbf{h} \quad \text{on } \Gamma_h \tag{4}$$

where, $\mathbf{n}$ is the unit normal vector on the boundary Γ. Here, Γ_g and Γ_h are the subsets of the boundary Γ. More details on the boundary conditions are given in Figure 1. The drag and lift force, (D, L), on the body can be calculated using the following expression:

$$(D, L)=\int_{\Gamma_B}\boldsymbol{\sigma}\mathbf{n}\,\mathrm{d}\Gamma \tag{5}$$

where, Γ_B represents the surface of the body.

2.2. The continuous adjoint approach

Let Γ_B be the segment of the boundary, Γ, whose shape is to be determined. Let $\boldsymbol{\beta}=(\beta_1,\ldots,\beta_m)$ be the set of shape parameters that govern its shape. Further, an objective function, $I_c(\mathbf{U},\boldsymbol{\beta})$, is defined that depends on the flow variables $\mathbf{U}=(\mathbf{u}, p)$ and shape parameters $\boldsymbol{\beta}$. The optimization problem involves determining the shape parameters that minimize (or maximize) the objective function, $I_c(\mathbf{U},\boldsymbol{\beta})$.

DOI: 10.1002/fld

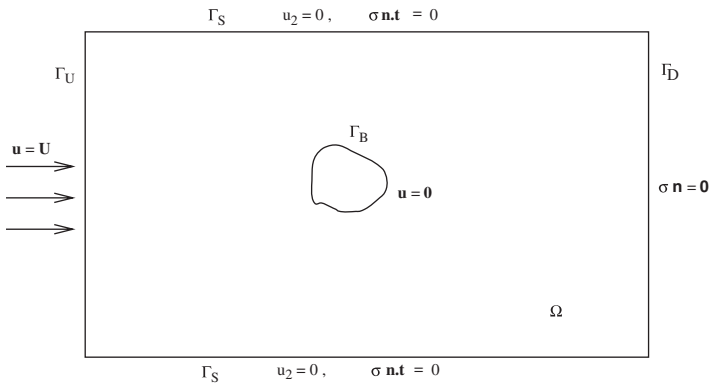

Figure 1. Schematic of the problem set-up: boundary conditions. Γ_U, Γ_D and Γ_S are the upstream, downstream and lateral boundaries, respectively and Γ_B is the body surface.

The flow Equations (1) and (2) may be written as $\Re = (\Re_{\mathbf{u}}, \Re_p)$, where $\Re_{\mathbf{u}}$ is the momentum equation and $\Re_p$ the continuity equation. These equations have to be satisfied for the flow variables $\mathbf{U} = (\mathbf{u}, p)$ that minimize (or maximize) the objective function, $I_c(\mathbf{U}, \boldsymbol{\beta})$. Therefore, the flow equations seem to appear as constraint conditions on the objective function. An augmented objective function is constructed to convert the constrained problem to an unconstrained one. The flow equations are augmented to the original objective function by introducing a set of Lagrange multipliers or adjoint variables, $\boldsymbol{\Psi} = (\boldsymbol{\psi}_{\mathbf{u}}, \psi_p)$.

$$I = I_c + \int_{\Omega} \Psi . \Re \, \mathrm{d}\Omega \tag{6}$$

It can be noticed that the augmented objective function degenerates to the original one if the flow variables, $\mathbf{U}$, satisfy Equations (1) and (2). Using principles of variational calculus, the variation of the augmented objective function is calculated as:

$$\delta I = \frac{\partial I}{\partial \mathbf{U}} \delta \mathbf{U} + \frac{\partial I}{\partial \boldsymbol{\beta}} \delta \boldsymbol{\beta} + \frac{\partial I}{\partial \boldsymbol{\Psi}} \delta \boldsymbol{\Psi} \tag{7}$$

It is seen from Equation (7) that δI depends on variations of $\mathbf{U}$, $\boldsymbol{\beta}$ and $\boldsymbol{\Psi}$. These variations are given as:

$$\frac{\partial I}{\partial \boldsymbol{\Psi}} = \Re(\mathbf{U}, \boldsymbol{\beta}) \tag{8}$$

$$\frac{\partial I}{\partial \mathbf{U}} = \left(\frac{\partial I_c}{\partial \mathbf{U}} + \int_{\Omega} \boldsymbol{\Psi}^{\mathrm{T}} \frac{\partial \Re}{\partial \mathbf{U}} \, \mathrm{d}\Omega \right) \tag{9}$$

$$\frac{\partial I}{\partial \boldsymbol{\beta}} = \left(\frac{\partial I_c}{\partial \boldsymbol{\beta}} + \int_{\Omega} \boldsymbol{\Psi}^{\mathrm{T}} \frac{\partial \Re}{\partial \boldsymbol{\beta}} \, \mathrm{d}\Omega \right) \tag{10}$$

The optimal solution is achieved when the variation of the augmented objective function vanishes, i.e. $\delta I = 0$. For this equation to be satisfied, the derivative of I with respect to each of the three

DOI: 10.1002/fld

parameters, i.e. the expressions in relations (8)–(10) should go to zero. Relation (8) leads to the flow Equations (1) and (2). Relation (9) results in the adjoint equations which can be utilized to compute the adjoint field. More details are given in the next section. The gradient of the augmented objective function, as given by relation (10), quantifies the sensitivity of the objective function with respect to the design parameters. It is utilized to refine the direction of search of the optimal shape parameters. The optimal solution is obtained when the gradient approaches zero.

2.3. Adjoint equations

The equations and boundary conditions for the adjoint variables are obtained by setting the expression given in (9) to zero. This leads to:

$$\rho(\nabla\mathbf{u})^{\mathrm{T}}\boldsymbol{\psi}_{\mathbf{u}}-\rho(\mathbf{u}.\nabla)\boldsymbol{\psi}_{\mathbf{u}}-\nabla.\boldsymbol{\sigma}_{\psi}=\mathbf{0} \quad \text{on } \Omega \tag{11}$$

$$\nabla.\boldsymbol{\psi}_{\mathbf{u}}=0 \quad \text{on } \Omega \tag{12}$$

where $\boldsymbol{\sigma}_{\psi}$ is similar to the stress tensor and is given by $\boldsymbol{\sigma}_{\psi}=-\psi_p\mathbf{I}+\mu[\nabla\boldsymbol{\psi}_{\mathbf{u}}+(\nabla\boldsymbol{\psi}_{\mathbf{u}})^{\mathrm{T}}]$. The variables $\boldsymbol{\psi}_{\mathbf{u}}$ and ψ_p are referred to as the adjoint velocity and adjoint pressure, respectively. Unlike the flow equations the equations for the adjoint variables are linear. The boundary conditions on the adjoint variables are:

$$\boldsymbol{\psi}_{\mathbf{u}}=\mathbf{0} \quad \text{on } \Gamma_U \tag{13}$$

$$\mathbf{s}=\mathbf{0} \quad \text{on } \Gamma_D \tag{14}$$

$$s_1=0, \quad \psi_{u2}=0 \quad \text{on } \Gamma_S \tag{15}$$

$$-\int_{\Gamma_B}\delta(\boldsymbol{\sigma}.\mathbf{n}).\boldsymbol{\psi}_{\mathbf{u}}\,\mathrm{d}\Gamma\,\mathrm{d}t+\frac{\partial I_c}{\partial\mathbf{u}}\delta\mathbf{u}+\frac{\partial I_c}{\partial p}\delta p=\mathbf{0} \quad \text{on } \Gamma_B \tag{16}$$

where, $\mathbf{s}=\{\mathbf{u}\boldsymbol{\psi}_{\mathbf{u}}-\psi_p+\mu[\nabla\boldsymbol{\psi}_{\mathbf{u}}+(\nabla\boldsymbol{\psi}_{\mathbf{u}})^{\mathrm{T}}]\}.\mathbf{n}$. Γ_U, Γ_D and Γ_S are the upstream, downstream and lateral boundaries and Γ_B is the body surface (see Figure 1). The boundary conditions on the surface of the body depend on the definition of the objective function. This is illustrated with an example. Let $I_c=\frac{1}{2}C_d^2$, where, C_d is the coefficient of drag acting on the body. This objective function is useful in designing a body that yields minimum drag coefficient. In this case, it can be shown that, the boundary conditions for the adjoint variables on the body surface given by Equation (16) can be simplified to:

$$\psi_{u1}=-C_d \quad \text{on } \Gamma_B \tag{17}$$

$$\psi_{u2}=0 \quad \text{on } \Gamma_B \tag{18}$$

3. FINITE ELEMENT FORMULATION

3.1. The flow equations

The domain Ω is discretized into elements Ω^e, $e=1,2,\ldots,n_{el}$, where n_{el} is the number of elements. Let $\mathscr{S}_u^h$ and $\mathscr{S}_p^h$ be the appropriate finite element spaces and $\mathscr{V}_u^h$ and $\mathscr{V}_p^h$ the weighing function spaces for velocity and pressure, respectively. The stabilized finite element formulation of

DOI: 10.1002/fld

Equations (1) and (2) is written as follows: find $\mathbf{u}^h \in \mathscr{S}_u^h$ and $p^h \in \mathscr{S}_p^h$ such that $\forall \mathbf{w}^h \in \mathscr{V}_u^h, q^h \in \mathscr{V}_p^h$,

$$\begin{aligned}
&\int_\Omega \mathbf{w}^h.\rho(\mathbf{u}.\nabla\mathbf{u}-\mathbf{f})\,\mathrm{d}\Omega+\int_\Omega \varepsilon(\mathbf{w}^h:\boldsymbol{\sigma}(p^h,\mathbf{u}^h))\,\mathrm{d}\Omega\\
&\quad+\int_\Omega q^h\,\nabla.\mathbf{u}^h\,\mathrm{d}\Omega+\sum_{e=1}^{n_{el}}\int_{\Omega^e}\frac{1}{\rho}(\tau_{SUPG}\rho\mathbf{u}^h.\nabla\mathbf{w}^h+\tau_{PSPG}\nabla q^h)\\
&\quad\cdot[\rho(\mathbf{u}.\nabla\mathbf{u}-\mathbf{f})-\nabla.\boldsymbol{\sigma}]\,\mathrm{d}\Omega^e+\sum_{e=1}^{n_{el}}\int_{\Omega^e}\tau_{LSIC}\nabla.\mathbf{w}^h\rho\nabla.\mathbf{u}^h\,\mathrm{d}\Omega^e\\
&=\int_{\Gamma^h}\mathbf{w}^h.\mathbf{h}^h\,\mathrm{d}\Gamma
\end{aligned}\tag{19}$$

The first three terms and the right-hand side in the variational formulation given by Equation (19) constitute the Galerkin formulation of the problem. The terms involving the element level integrals are the stabilization terms added to the basic Galerkin formulation to enhance its numerical stability. These terms stabilize the computations against node-to-node oscillations in advection dominated flows and allow the use of equal-in-order basis functions for velocity and pressure. The terms with coefficients τ_{SUPG} and τ_{PSPG} are based on the SUPG (Streamline-Upwind/Petrov-Galerkin) and PSPG (Pressure-stabilized/Petrov-Galerkin) method [27]. The term with coefficient τ_{LSIC} is also a stabilization term based on the least squares of the incompressibility constraint and is found to be useful for large Reynolds number flows. Equal-in-order basis functions for velocity and pressure, that are linear in space (three-noded triangular elements) are used. A three point quadrature is employed for numerical integration.

3.2. The adjoint equations

A stabilized SUPG/PSPG finite element method is proposed to solve the adjoint Equations (11) and (12). Let $\mathscr{S}^h_{\boldsymbol{\psi}_\mathbf{u}}$ and $\mathscr{S}^h_{\psi_p}$ be the appropriate finite element spaces and $\mathscr{V}^h_{\boldsymbol{\psi}_\mathbf{u}}$ and $\mathscr{V}^h_{\psi_p}$ the corresponding weighting function spaces for the adjoint velocity and adjoint pressure. The stabilized finite element formulation of Equations (11) and (12) is written as follows: given $\mathbf{u}^h$ and $\mathbf{p}^h$ satisfying Equations (1) and (2), find $\boldsymbol{\psi}^h_\mathbf{u} \in \mathscr{S}^h_{\boldsymbol{\psi}_\mathbf{u}}$ and $\boldsymbol{\psi}^h_p \in \mathscr{S}^h_{\psi_p}$ such that $\forall \mathbf{w}^h_{\boldsymbol{\psi}_\mathbf{u}} \in \mathscr{V}^h_{\boldsymbol{\psi}_\mathbf{u}}, q^h_{\psi_p} \in \mathscr{V}^h_{\psi_p}$,

$$\begin{aligned}
&\int_\Omega \mathbf{w}^h_{\boldsymbol{\psi}_\mathbf{u}}.\rho((\nabla\mathbf{u}^\mathbf{h})^\mathrm{T}\boldsymbol{\psi}^h_\mathbf{u}-\mathbf{u}.\nabla\boldsymbol{\psi}_\mathbf{u})\,\mathrm{d}\Omega+\int_\Omega \varepsilon(\mathbf{w}^h_{\boldsymbol{\psi}_\mathbf{u}}):\boldsymbol{\sigma}_\psi(\psi^h_p,\boldsymbol{\psi}^h_\mathbf{u})\,\mathrm{d}\Omega\\
&\quad+\int_\Omega q^h_{\psi_p}\,\nabla.\boldsymbol{\psi}^h_\mathbf{u}\,\mathrm{d}\Omega+\sum_{e=1}^{n_{el}}\int_{\Omega^e}\frac{1}{\rho}(-\tau_{SUPG}\rho\mathbf{u}^h.\nabla\mathbf{w}^h_{\boldsymbol{\psi}_\mathbf{u}}+\tau_{PSPG}\nabla q^h_{\psi_p})\\
&\quad\cdot[\rho((\nabla\mathbf{u}^\mathbf{h})^\mathrm{T}\boldsymbol{\psi}^h_\mathbf{u}-\mathbf{u}.\nabla\boldsymbol{\psi}_\mathbf{u})-\nabla.\boldsymbol{\sigma}_\psi(\psi^h_p,\boldsymbol{\psi}^h_\mathbf{u})]\,\mathrm{d}\Omega^e\\
&\quad+\sum_{e=1}^{n_{el}}\int_{\Omega^e}\tau_{LSIC}\nabla.\mathbf{w}^h_{\boldsymbol{\psi}_\mathbf{u}}\rho\nabla.\boldsymbol{\psi}^h_\mathbf{u}\,\mathrm{d}\Omega^e=\mathbf{0}
\end{aligned}\tag{20}$$

DOI: 10.1002/fld

The stabilization coefficients τ_{SUPG}, τ_{PSPG} and τ_{LSIC} in the formulation proposed in Equation (20) are computed based on the flow variables $(\mathbf{u}, p)$.

4. PARAMETRIZATION

The form of parametrization determines the choice of the design variables. To carry shape optimization one would like to have a parametrization that offers a rich design space. In the present work NURBS (Non-Uniform Rational B-Splines) [29] have been used to parametrize the airfoil geometry. A NURBS curve is defined as:

$$\mathbf{C}(t) = \frac{\sum_{i=0}^{n} N_{i,p}(t) w_i \mathbf{P}_i}{\sum_{i=0}^{n} N_{i,p}(t) w_i} \tag{21}$$

Here, n is the number of control points, p is the order of the curve, t is the knot vector, w_i is the weight associated with control point $\mathbf{P}_i$ and $N_{i,p}$ are the B-Spline basis functions given by:

$$N_{i,0} = \begin{cases} 1 & \text{if } t_i \leqslant t \leqslant t_{i+1} \\ 0 & \text{otherwise} \end{cases} \tag{22}$$

$$N_{i,p} = \frac{t - t_i}{t_{i+p} - t_i} N_{i,p-1}(t) + \frac{t_{i+p+1} - t}{t_{i+p+1} - t_{i+1}} N_{i+p,p-1}(t) \tag{23}$$

A wide range of curves can be obtained by changing the location and weight of the control points or by changing the knot sequence. In the present work a 4th order NURBS curve with 13 control points is used to model the surface of the airfoil. Figure 2 shows an example of an attempt to model a NACA 0012 airfoil. As seen from the figure, the control points 1 and 13 are identical resulting in a closed curve and an airfoil with sharp trailing edge. In addition, the leading and trailing edge of the airfoil are fixed to achieve the desired chord length and angle of attack. This allows us to utilize the remaining 10 control points as design variables. In the present work only the y-coordinates of the control points are allowed to move. Each of the design variable is allowed to change between a lower and a upper bound that is specified a priori. The maximum value a design variable is allowed to change to ($\mathbf{y}_{\min}^{low}$ and $\mathbf{y}_{\max}^{up}$) is shown in Figure 2. The superscripts 'low' and 'up' refer to the lower and upper surface of airfoil, respectively. In this study $\mathbf{y}_{\min}^{low}$ and $\mathbf{y}_{\max}^{up}$ are set to -0.2 and 0.4 respectively. The other bounds ($\mathbf{y}_{\max}^{low}$ and $\mathbf{y}_{\min}^{up}$) are set so that the lower and upper surfaces do not cross each other.

5. THE OPTIMIZER

The optimization algorithm used in the present work is the L-BFGS (Limited memory-Broyden-Fletcher-Goldfarb-Shanno) procedure [28]. This is a limited memory quasi-Newton method for solving large nonlinear optimization problems that are constrained by upper and lower bounds on the design variables. The algorithm is well suited for problems when the information for the second derivative (the Hessian) is difficult to obtain.

DOI: 10.1002/fld

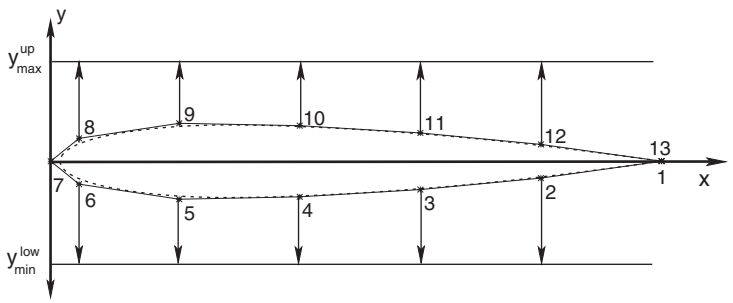

Figure 2. Parametrization of a NACA 0012 airfoil using 4th order NURBS curve with 13 controls points. The y-coordinates of the control points 2–6 and 8–12 are used as design variables for optimizing the airfoil. The airfoil surface is shown in broken lines. Upper bounds of the design variables on the upper surface ($\mathbf{y}^{up}_{\max}$) and the lower bounds of the design variables on the lower surface ($\mathbf{y}^{low}_{\min}$) are also shown.

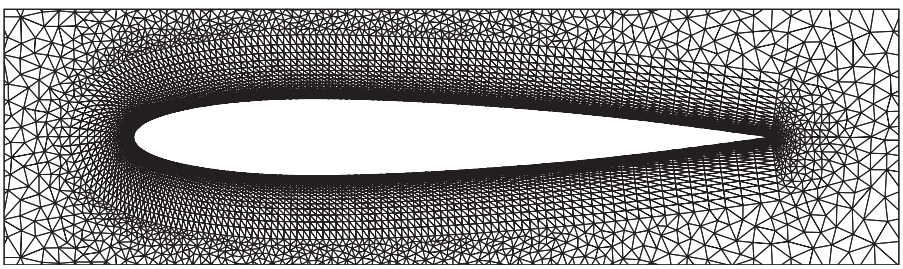

Figure 3. Close-up view of the finite element mesh for the NACA 0012 airfoil at 0° angle of attack. The mesh consists of 9828 nodes and 19366 triangular elements. The surface of the airfoil is discretized using 200 nodes.

6. THE FINITE ELEMENT MESH

An airfoil of unit chord length is placed in a domain whose outer boundary is a rectangle. The upstream and downstream boundaries are located at 20 chord lengths, each, from the trailing edge of the airfoil. The lateral boundaries are placed at 10 chord length, each, from the airfoil. A typical finite element mesh used for computation is shown in Figure 3. It consists of 9883 nodes and 19 366 triangular elements with 200 nodes on the surface of the airfoil. Close to the airfoil surface a structured mesh is employed to resolve the boundary layer flow. The remaining domain is discretized using an unstructured mesh via Delaunay triangulation.

6.1. Mesh convergence study

Two meshes (M1 and M2) are used to compute the flow over the NACA 0012 airfoil at at $\alpha = 4°$ and $Re = 250$. The details of the meshes are given in Table I. The drag and lift coefficients obtained for the NACA 0012 are also tabulated. Meshes M1 and M2 are used to obtain an optimal airfoil having the largest lift coefficient at $Re = 250$. Both the meshes led to the same final shape whose aerodynamic coefficients are also tabulated in Table I. The optimal solution is discussed later in

DOI: 10.1002/fld

Table I. The lift and drag coefficients of the NACA 0012 airfoil and the optimal airfoil at $\alpha=4^\circ$ and $Re=250$ for two finite element meshes.

Mesh	Nodes	Elements	C_d(NACA0012)	C_l(NACA0012)	C_d(Optimal)	C_l(Optimal)
M1	9828	19366	0.2563	0.2248	0.2834	0.4870
M2	22872	45338	0.2561	0.2243	0.2829	0.4874

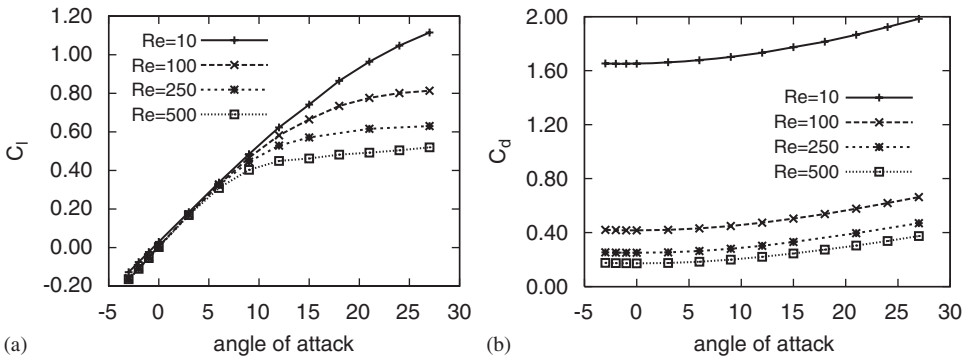

Figure 4. Flow past NACA 0012 airfoil at low Reynolds numbers: variation of (a) lift coefficient and (b) drag coefficient with angle of attack.

the paper. Since the difference in the aerodynamic coefficients from the two meshes is less than 0.3%, mesh M1 is used for further computations.

7. FLOW PAST A NACA 0012 AIRFOIL

First we investigate the steady flow past a typical conventional airfoil for $Re\leqslant 500$. The variation of the lift and drag coefficients with respect to the angle of attack for the NACA 0012 airfoil is shown in Figure 4. At each α the drag coefficient decreases with increase in Re. The variation of the lift coefficient is approximately linear with α for low values of angle of attack. The departure from linearity occurs at $\alpha\simeq 12^\circ$ for $Re=10$. With increase in Re the range of Re for which the linear behavior is observed decreases. For example, at $Re=500$, the $C_l-\alpha$ variation exhibits non-linear behavior for α beyond 6°. At angles of attack beyond the linear range the lift curve slope gradually decreases. Unlike the stall behavior observed at very large Re, at low Re, the $C_l-\alpha$ variation remains monotonic.

The variation of the lift and drag coefficient at $\alpha=4^\circ$ with Re is shown in Figure 5. The drag coefficient decreases monotonically with increase in Re. The lift coefficient, on the other hand, exhibits a non-monotonic variation. It decreases with Re for $Re<50$ and then shows an increasing trend for $50\leqslant Re\leqslant 175$. For $Re>175$, C_l decreases with increase in Re. To investigate this behavior we study the variation of the pressure and viscous contribution to the lift with Re. This is shown in Figure 6. The pressure contribution to the lift coefficient shows a monotonic decreasing trend with Re. On the other hand, the viscous contribution increases monotonically with Re. In fact, it is negative for $Re<100$. The summation of the two contributions results in a non-monotonic

DOI: 10.1002/fld

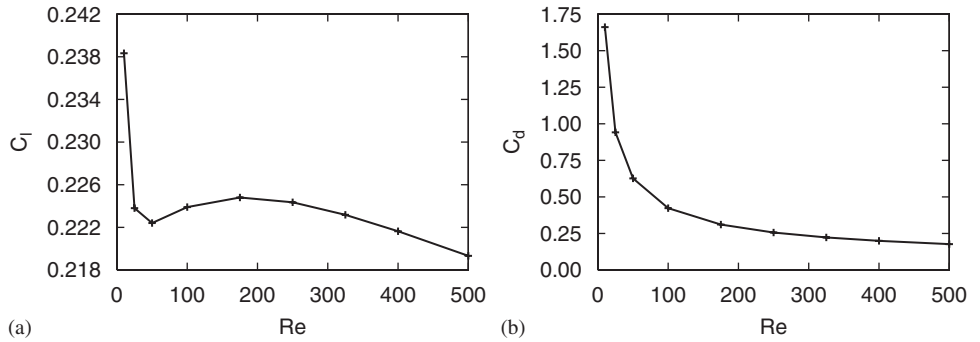

Figure 5. Flow past a NACA 0012 airfoil at $\alpha = 4°$: variation of the lift and drag coefficients with *Re*.

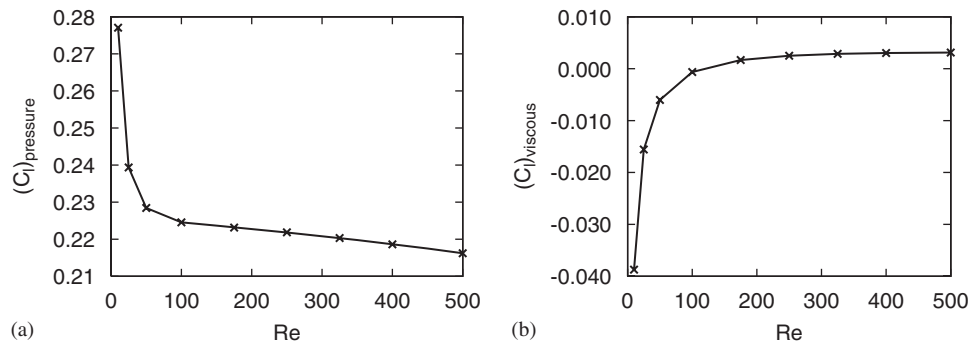

Figure 6. Flow past a NACA 0012 airfoil at $\alpha = 4°$: pressure and viscous contribution to the lift coefficient with *Re*.

variation of overall C_l with *Re*. The variation of the lift and drag coefficients at $\alpha = 12°$ with *Re* is shown in Figure 7. Unlike at $\alpha = 4°$, both, the drag and lift coefficients decrease monotonically with increase in *Re*. The variation of C_l with *Re* is more significant at $\alpha = 12°$ as compared to the one at $\alpha = 4°$.

8. SHAPE OPTIMIZATION

The results presented in the previous section show that the flow past an airfoil is very sensitive to *Re*. We now attempt to seek optimal shape of an airfoil at various *Re* in the regime of steady laminar flow. The airfoil is parametrized via a 4th order NURBS curve with 10 control points as design parameters. A mesh moving scheme [26] is utilized to deform the mesh to adopt to a new airfoil geometry. The initial guess for the design cycle is the NACA 0012 airfoil. The optimization study is carried out with and without a constraint on the volume enclosed by the airfoil.

DOI: 10.1002/fld

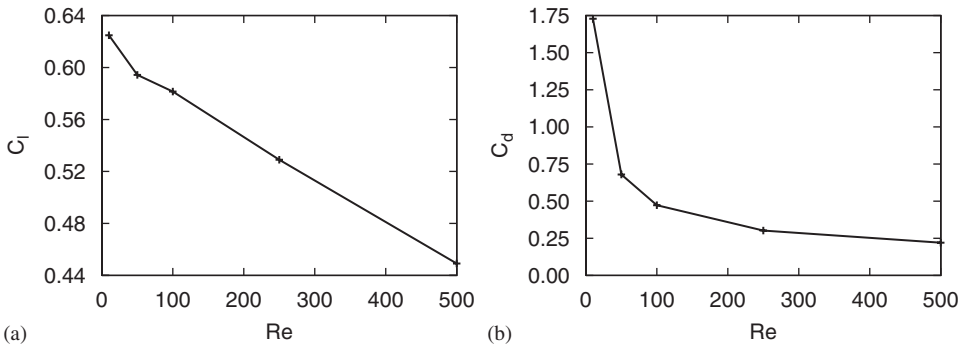

Figure 7. Flow past a NACA 0012 airfoil at $\alpha = 12°$: variation of the lift and drag coefficients with *Re*.

8.1. Shape optimization with no constraint on volume

A good airfoil is expected to yield high lift and low drag. In this work we investigate the relative performance of several objective functions in a design cycle. Five objective functions $(I_1, I_2, I_3, I_4, I_5)$ are considered. They are given as:

$$I_1 = +\tfrac{1}{2}C_d^2 \tag{24}$$

$$I_2 = -\tfrac{1}{2}C_l^2 \tag{25}$$

$$I_3 = -\frac{1}{2}\left(\frac{C_l}{C_d}\right)^2 \tag{26}$$

$$I_4 = -\tfrac{1}{2}C_l^2 + \tfrac{1}{2}C_d^2 \tag{27}$$

$$I_5 = +\tfrac{1}{2}C_d^2 + \tfrac{1}{2}(C_l - C_l^\circ)^2 \tag{28}$$

The objective function, I_1, minimizes the drag coefficient, I_2 maximizes the lift coefficient while I_3 maximizes the lift to drag ratio. The fourth objective function, I_4, maximizes the lift coefficient and minimizes the drag coefficient, simultaneously. The fifth objective function, I_5, minimizes the drag coefficient while the lift coefficient is held constant at a value of C_l°.

8.1.1. $\alpha = 4°$. *Minimizing* $C_d(I_1)$: At zero angle of attack, of all the possible airfoils of given chord length, the flat plate results in the smallest drag. Here, we wish to find out as to what the optimal shape is for non-zero angle of attack. The first column of Figure 8 shows the final shapes obtained at various *Re*. A thin curved surface is obtained at all *Re*. This is the thinnest possible shape that the present parametrization can provide. The shape parameters have been assigned constraints so that the upper and lower surfaces do not cross each other and lead to a breakdown of the computation. Compared to a NACA 0012 airfoil the final geometry shows a reduction in drag of 7% and 10.5%, approximately, at $Re = 10$ and 500. The C_l, C_d and C_l/C_d of the optimal shapes at various *Re* are listed in Table II.

Maximizing $C_l(I_2)$: The final shapes obtained with objective function I_2 at various *Re* are shown in the second column of Figure 8. Except at $Re = 10$, at all other *Re*, shape parameters on the lower

DOI: 10.1002/fld

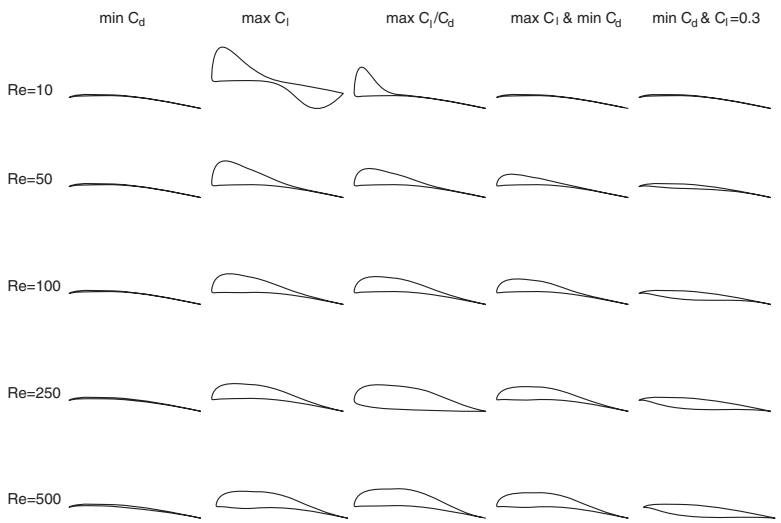

Figure 8. Optimal airfoil shapes obtained with objective functions I_1, I_2, I_3, I_4 and I_5 at various Re. The angle of attack is 4°.

Table II. Drag and lift coefficients of the final shapes at $\alpha = 4°$ obtained using various objective functions at different Re.

	10		50		100		250		500	
Re	C_d	C_l	C_d	C_l	C_d	C_l	C_d	C_l	C_d	C_l
NACA 0012	1.661	0.238	0.627	0.222	0.423	0.224	0.256	0.224	0.178	0.219
I_1	1.542	0.362	0.567	0.413	0.380	0.452	0.229	0.501	0.159	0.527
I_2	1.967	0.663	0.700	0.524	0.461	0.500	0.283	0.487	0.203	0.419
I_3	1.796	0.605	0.650	0.512	0.447	0.500	0.290	0.263	0.212	0.397
I_4	1.542	0.362	0.615	0.487	0.433	0.508	0.271	0.488	0.198	0.443
I_5	1.542	0.362	0.572	0.377	0.389	0.351	0.238	0.329	0.165	0.319

surface of the airfoil reach their specified upper bounds. At $Re \geqslant 50$ the optimal shapes appear to be very similar to that of a conventional airfoil. However, the shape at $Re = 10$ is quite different. It has high thickness close to the leading and trailing edges and the maximum thickness to chord ratio is larger than 40%. Compared to NACA 0012 airfoil it results in a 178% increase in lift coefficient. The pressure distribution of the optimal airfoil along with that of the NACA 0012 airfoil is shown in Figure 9. The peak suction on the optimal airfoil is much larger. Also, the pressure on the lower surface is higher for the optimal airfoil, compared to that on NACA 0012 airfoil. This leads to enhanced lift on the optimal airfoil geometry. The flow and adjoint fields for the final shape at $Re = 10$ are shown in Figure 10. The flow remains attached over the entire chord length. With increase in Re the maximum thickness of the airfoil decreases. To see whether the final shapes obtained are global or local optima, a different initial guess is used to obtain the optimal shape at $Re = 250$. The final shapes obtained along with the different initial guesses are shown in Figure 11.

DOI: 10.1002/fld

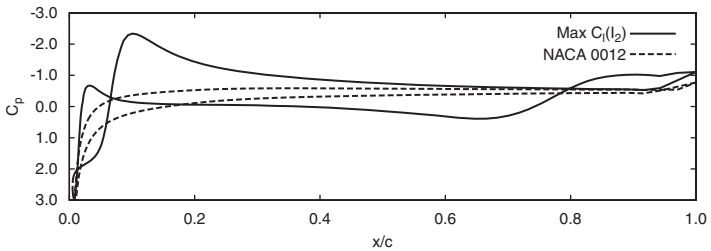

Figure 9. Pressure distribution of the optimal airfoil obtained with objective function I_2 at $Re = 10$ and $\alpha = 4°$.

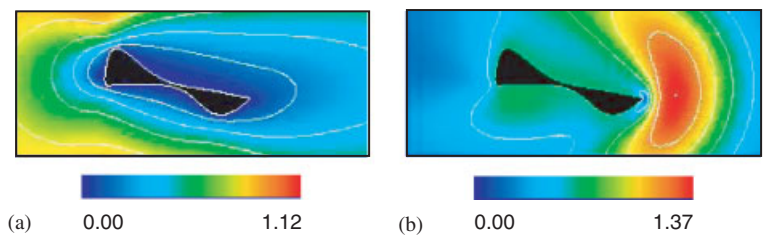

Figure 10. Optimal shape for maximization of the lift coefficient at $\alpha = 4°$, $Re = 10$: (a) magnitude of the flow velocity and (b) magnitude of adjoint velocity.

Compared to the final shape obtained by using NACA 0012 airfoil, the other shape generates 8.5% lesser lift. In both the cases all the control points on the lower surface reach their specified upper bounds. Only the control points on the upper surface adapt to give an optimal shape. The existence of two optima suggests the possibility of the lift coefficient being an oscillatory function of the design variable having multiple local optima. To understand this further, the variation of the lift coefficient with the design variables is obtained for both the optimal shapes. Only control point 8, as shown in Figure 2, is allowed to move. The variation of the lift coefficient with location of the control point is shown in Figure 12. The variation is seen to be non-monotonic and different for both the shapes, thereby confirming the existence of more than one local optima. The lift and drag coefficients of the optimal airfoil at various *Re* are listed in the third row of Table II. The iteration history of the lift and drag coefficient is shown in Figure 13. In most cases $10-15$ iterations in the design cycle are enough to achieve the desired objective.

Maximizing $C_l/C_d(I_3)$: The final shapes obtained with objective function I_3 are shown in the third column of Figure 8. At $Re = 10$, an airfoil with a bulbous leading edge followed by a thin curved surface is obtained. This shape has a lift to drag ratio that is 135% more than that of a NACA 0012 airfoil. With increase in *Re* the extent of the thin curved surface decreases. For $Re = 250$ and $Re = 500$ the C_l/C_d for the shapes at the end of the design cycle is only marginally higher than that of NACA 0012 airfoil. The present optimization algorithm can only locate the closest local maxima/minima. Computation with different initial guesses lead to geometries with better C_l/C_d. However, those results are not being shown here as we wish to compare the performance of all

DOI: 10.1002/fld

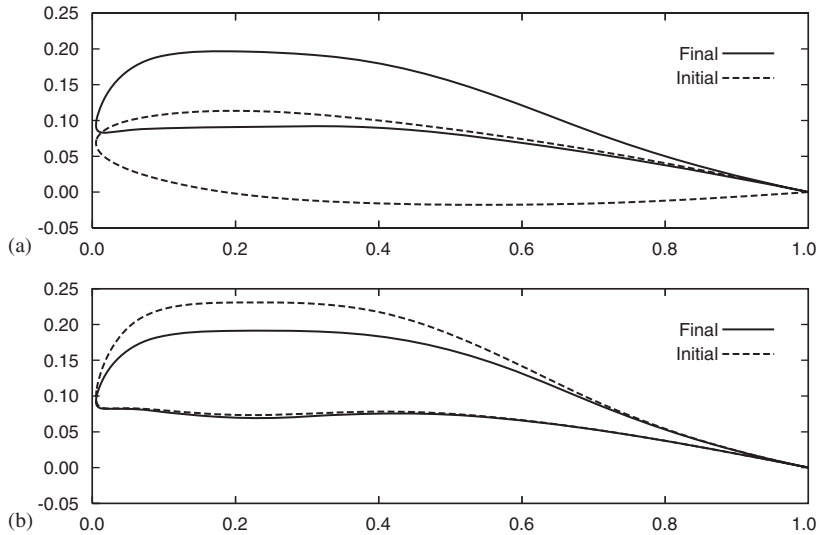

Figure 11. Optimal shapes obtained with two different initial guesses for maximization of the lift coefficient at $\alpha = 4°$, $Re = 250$.

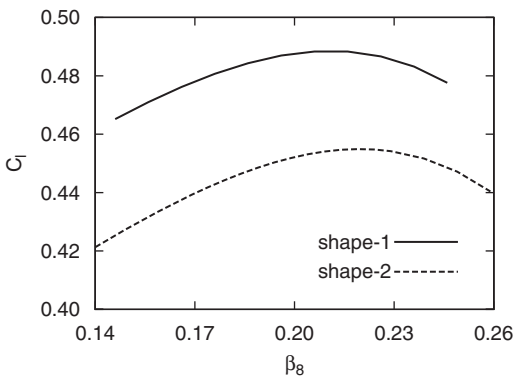

Figure 12. Variation of the lift coefficient with respect to control point 8 (as shown in Figure 2) for the final shape obtained using objective function I_2 at $\alpha = 4°$, $Re = 250$.

the objective functions with respect to same initial guess. The lift and drag coefficients of the final shapes are listed in second last row of Table II.

Maximizing C_l and minimizing C_d(I_4): The objective function I_4 consists of two terms. Depending on the relative size of the terms their contribution to the objective function is different. For the NACA 0012 airfoil the lift to drag ratio is less than unity for $Re = 10$ and larger than unity for $Re = 500$. Therefore, at low Re, it is expected that the objective function I_4 will have more relative weightage on minimizing C_d than on maximizing C_l. Similarly, at $Re = 500$ it is expected

DOI: 10.1002/fld

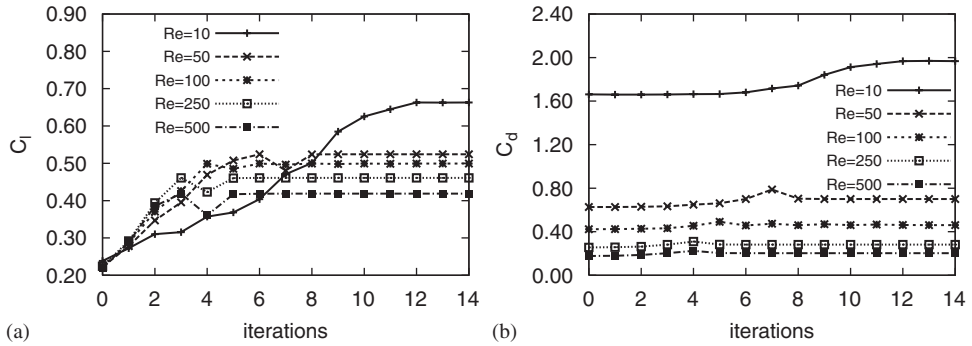

Figure 13. Maximization of the lift coefficient at $\alpha = 4°$: (a) iteration history of the lift coefficient and (b) drag coefficient.

that maximizing C_l will contribute relatively more to I_4 than minimizing C_d. The final shapes with objective function I_4 are shown in the fourth column of Figure 8. The optimal shape at $Re = 10$ is a thin curved surface, similar to the shape obtained using objective function I_1. The optimal shape at $Re = 500$ has a C_l that is twice that of the NACA 0012 airfoil and the shape is closer to that obtained with maximizing C_l. The lift and drag coefficients of the finals shapes are listed in the second last row of Table II.

Minimizing C_d for a specified $C_l(I_5)$: The objective function I_5 is a combination of a direct and an inverse objective function [18]. This function seeks a surface that has the least drag coefficient and a specified lift coefficient, $C_l = C_l^\circ$. Similar to I_4, the contribution of the two terms to the objective function is different. For $\alpha = 4°$, C_l° is specified to be 0.3. The fifth column of Figure 8 shows the final shapes obtained with this objective function. For all the *Re* considered, the direct objective contributes more than the inverse objective to I_5. At $Re = 10$, the final shape obtained is similar to the one obtained from I_1. With increase in *Re* the contribution of the drag component decreases. The thickness of the optimal shape increases with increase in *Re*. The lift coefficient approaches the desired lift coefficient with increase in *Re*. The drag at all *Re* is lesser than that for NACA 0012 airfoil. The lift and drag coefficients of the final shapes are tabulated in the last row of Table II.

Relative performance of various objective functions: Figure 14 shows the summary of the aerodynamic coefficients obtained with different objective functions at $\alpha = 4°$ and various *Re*. One would expect that at each *Re*, amongst the four shapes obtained with different objective functions the one obtained with I_2 should result in maximum lift. Similarly, the shape obtained with I_1 should result in minimum C_d and the one obtained with I_3 should give maximum C_l/C_d. Figure 14 shows some surprising results. At $Re = 100$, I_4 leads to maximum C_l. Also the maximum C_l/C_d is produced by the shape resulting from I_1 and not from I_3, for $Re \geqslant 100$. The objective function I_5 does not produce any non-intuitive result. Using I_5, it is possible to obtain a shape having the desired lift coefficient. However, this would require assigning suitable relative weights to the two terms in the objective function.

8.1.2. $\alpha = 12°$. *Minimizing* $C_d(I_1)$: The final shapes obtained with objective function I_1 at $\alpha = 12°$ are shown in the first column of Figure 15. As is the case at $\alpha = 4°$, a thin curved surface is obtained at $Re = 10$ and 50. At $Re = 100$, 250 and 500 the optimal shapes are thicker. They have a negative

DOI: 10.1002/fld

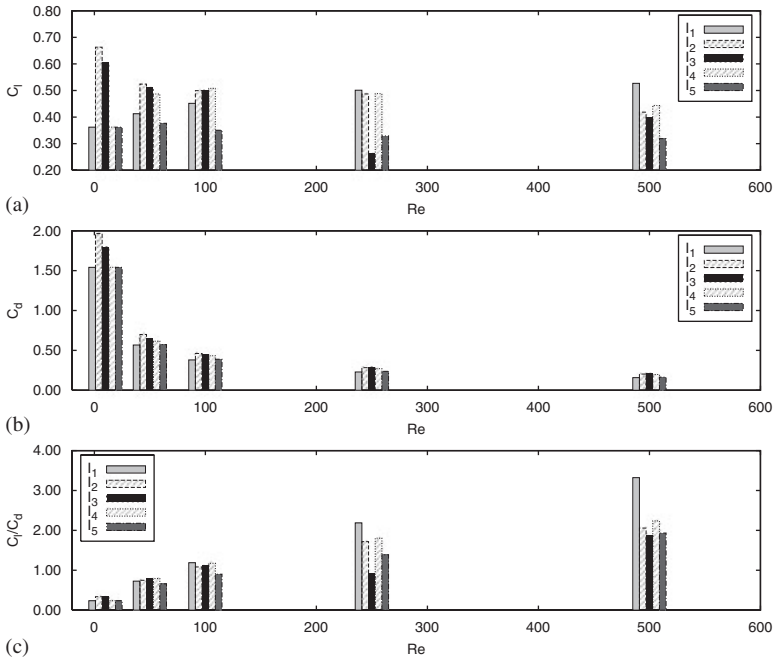

Figure 14. Aerodynamic coefficients of the final shapes obtained from the considered objective function at $\alpha = 4^\circ$: (a) lift coefficient; (b) drag coefficient; and (c) lift to drag ratio.

camber which increases with increase in Re. It is somewhat surprising that the optimal shape at $Re = 500$ is thicker than the one at $Re = 10$. To study the this we investigate the flow at $Re = 500$ for three geometries: (a) NACA 0012 airfoil (b) the optimal airfoil obtained at $Re = 500$ and (c) the optimal airfoil obtained at $Re = 10$. The pressure and viscous components of drag for these geometries are listed in Table III. The optimal airfoil for $Re = 500$ has lesser drag than the thin airfoil obtained as an optimal solution at $Re = 10$. The pressure component of the drag is 4% lesser while the viscous component is only about 1% lesser. The flow and the adjoint fields over the final shape at $Re = 500$ are shown in Figure 16. The lift and drag coefficients of the optimal shapes at all the Re studied are shown in Figure 17 and listed in Table IV.

Maximizing $C_l(I_2)$: The final shapes obtained with objective function I_2 are shown in second column of Figure 15. At $Re = 10$, an airfoil with a small bulbous leading edge followed by a thin curved surface is obtained. With increase in Re, the location of the maximum thickness moves aft of the leading edge. The optimal shape at $Re = 500$ is similar to that of a conventional airfoil. The optimal shape at $Re = 10$ has 45% more C_l than NACA 0012 airfoil while at $Re = 500$ the increase in C_l is only 30%. The lift and drag coefficients are listed in Table IV.

Maximizing $C_l/C_d(I_3)$: The final shapes obtained with objective function I_3 are shown in the third column of Figure 15. Except at $Re = 10$, a thin curved surface is obtained at all other Re. At $Re = 10$ the final shape has 39% more C_l/C_d than NACA 0012 airfoil while at $Re = 500$ an increase of 87% is obtained. At $Re = 500$ the shapes resulting from I_1 and I_3 are quite different. Yet, interestingly the drag coefficients associated with the two shapes are very similar. The lift and drag coefficients for shapes obtained with I_3 are listed in the second last row of Table IV.

DOI: 10.1002/fld

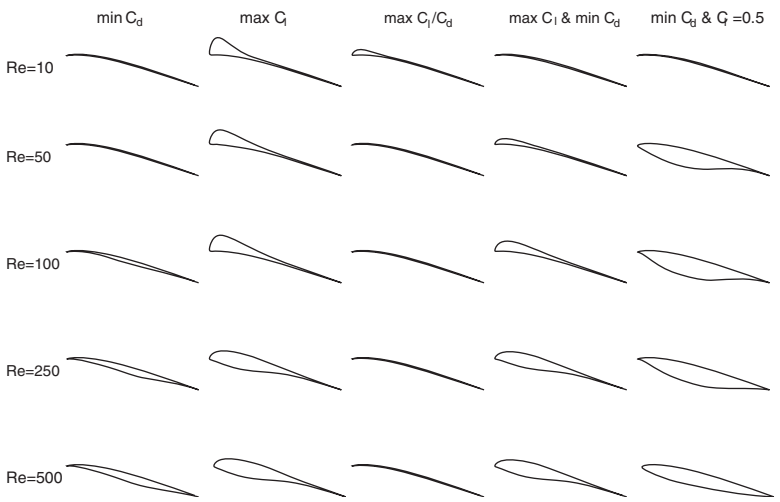

Figure 15. Optimal airfoil shapes obtained with objective functions I_1, I_2, I_3, I_4 and I_5 at various Re. The angle of attack is 12°.

Table III. $Re=500$, $\alpha=12°$ flow past an airfoil: comparison of the pressure and viscous components of the drag coefficient for various shapes, (a) NACA 0012 airfoil (b) optimal airfoil for $Re=500$ and (c) optimal airfoil for $Re=10$.

S.No.	Shape	C_d (pressure)	C_d (viscous)
(a)	NACA 0012	0.11498	0.10477
(b)	Optimal airfoil (min C_d) for $Re=500$	0.11386	0.10158
(c)	Optimal airfoil (min C_d) for $Re=10$	0.11849	0.10223

Maximizing C_l and minimizing C_d(I_4): The final shapes obtained with objective function I_4 are shown in the fourth column of Figure 15. The lift and drag coefficients are listed in the second to last row of Table IV. At $Re=10$, C_d decreases by 4.7% and C_l increases by 30% while at $Re=500$ both C_d and C_l increase by 6.1% and 36.5%, respectively. If the objective is to maximize lift and minimize drag, simultaneously then both the terms in the objective function, I_4, should have comparable contributions. As is seen at $\alpha=4°$, the lift to drag ratio of the NACA 0012 airfoil at $\alpha=12°$ varies from less than unity at $Re=10$ to more than unity at $Re=500$. Therefore at low Re, the shapes resulting from I_4 are same as that from minimizing drag, at $Re=500$, the shapes from I_4 and I_2 are very similar.

Minimizing C_d at specified C_l°(I_5): The final shapes obtained with objective function I_5 are shown in the fifth column of Figure 15. The desired lift coefficient C_l° is specified to be 0.5. Similar to the results at $\alpha=4°$, the final shape at $Re=10$ is a thin curved plate akin to the result obtained using I_1. At higher Re, with the continuously decreasing contribution of the drag to the objective function, the lift coefficient is seen to approach the desired lift. The lift and drag coefficients of the final shapes are listed in the last row of Table IV.

DOI: 10.1002/fld

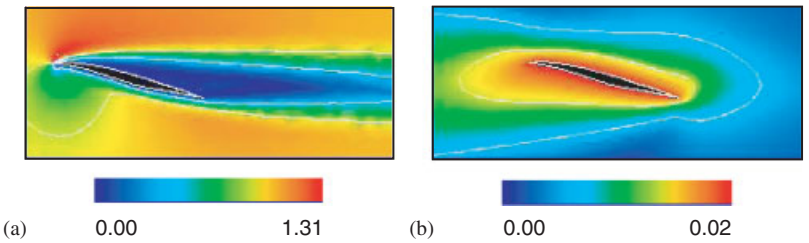

Figure 16. Optimal shape while minimizing the drag coefficient at $\alpha = 12°$, $Re = 500$: (a) magnitude of the flow velocity (b) magnitude of adjoint velocity.

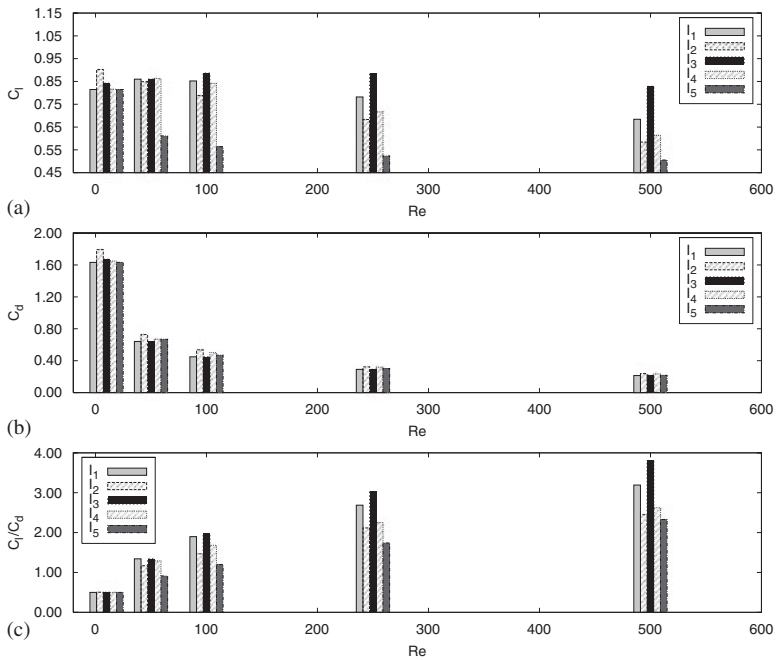

Figure 17. Aerodynamic coefficients of the final shapes obtained from the considered objective function at $\alpha = 12°$: (a) lift coefficient (b) drag coefficient and (c) lift to drag ratio.

Relative performance of various objective functions: Figure 17 shows the variation of the aerodynamic coefficients with *Re* obtained with different objective functions. As is observed at $\alpha = 4°$, least C_d is produced by the shapes arising from objective function I_1. However, the airfoil with largest C_l does not always come from the satisfaction of I_2. For example, at $Re \geqslant 100$ I_3 results in shapes with highest C_l. The largest C_l/C_d is mostly produced by shapes that are outcome of I_3. As expected, I_4 results in shapes that resemble the ones from I_1 at low *Re* and those that look like the ones from I_2 at larger *Re*. I_5 does not lead to any interesting solution, unless suitable relative weights are defined for the two terms in the objective function. Therefore, the use of I_4 and I_5 do not seem to add any useful information and are dropped in the remaining study.

DOI: 10.1002/fld

Table IV. Drag and lift coefficients of the final shapes at $\alpha = 12^\circ$ obtained using various objective functions at different *Re*.

	10		50		100		250		500	
Re	C_d	C_l	C_d	C_l	C_d	C_l	C_d	C_l	C_d	C_l
NACA 0012	1.728	0.625	0.679	0.594	0.473	0.582	0.302	0.529	0.221	0.449
I_1	1.632	0.815	0.641	0.860	0.449	0.852	0.291	0.782	0.214	0.684
I_2	1.792	0.903	0.728	0.849	0.537	0.788	0.323	0.683	0.238	0.584
I_3	1.672	0.842	0.641	0.860	0.449	0.886	0.292	0.884	0.218	0.829
I_4	1.647	0.816	0.669	0.863	0.5	0.842	0.318	0.716	0.234	0.613
I_5	1.632	0.815	0.669	0.612	0.470	0.564	0.301	0.524	0.217	0.504

8.2. Shape optimization with volume constraint

A geometric constraint is added to the objective functions. We now seek to generate airfoil shapes that enclose a prescribed volume. The following modified objective functions are considered:

$$I_{v1} = \tfrac{1}{2}C_d^2 + \gamma\tfrac{1}{2}(V - V_o)^2 \tag{29}$$

$$I_{v2} = -\tfrac{1}{2}C_l^2 + \gamma\tfrac{1}{2}(V - V_o)^2 \tag{30}$$

$$I_{v3} = -\frac{1}{2}\left(\frac{C_l}{C_d}\right)^2 + \gamma\frac{1}{2}(V - V_o)^2 \tag{31}$$

where V_o is the volume enclosed by NACA 0012 airfoil and γ is the relative weight factor for the two objectives. It has been our experience that if γ is too small, the volume constraint is not adequately satisfied while if it is too large the aerodynamic constraint does not yield the best results. The computations were carried out for various values of γ. The results reported here are for $\gamma = 1000$ for I_{v1} and I_{v2} and $\gamma = 10000$ for I_{v3}. The objective function I_4 is dropped in this study because it has been shown not to lead to results that are better than the ones obtained with I_1–I_3. These objective functions are a mix of a direct and inverse problems. The volume constraint is inverse in nature while the aerodynamic contribution to the objective function is direct in nature.

8.2.1. $\alpha = 4^\circ$. Figure 18 shows the final shapes obtained with with various objective functions. The first column shows the shapes obtained with I_{v1}. The final shapes at various *Re* are seen to have negative camber. The optimal shape at $Re = 10$ shows 1.5% reduction in C_d compared to a NACA 0012 airfoil, while the reduction observed at $Re = 500$ is 1%. The final shapes obtained with objective function I_{v2} are shown in the second column of Figure 18. Similar to the case without any constraints, the final shape at $Re = 10$ has a thickness to chord ratio of over 40% with high thickness close to the leading and trailing edges. Compared to the NACA 0012 airfoil, the final shape at $Re = 10$ has 178% more lift while at $Re = 500$ the increase is 94%. The shapes for $Re = 50$ to 250 have an upper surface with a slight dimple at around 20% chord. To investigate the reason for this occurrence, the optimal shape at $Re = 250$ is slightly modified and studied. The upper surface of the optimal airfoil obtained at $Re = 250$ is straightened to remove the dimple. It is seen that the original optimal airfoil has 3% larger lift coefficient than the modified airfoil. The optimal airfoil and the modified airfoil are shown in Figure 19 along with their pressure distribution. The

DOI: 10.1002/fld

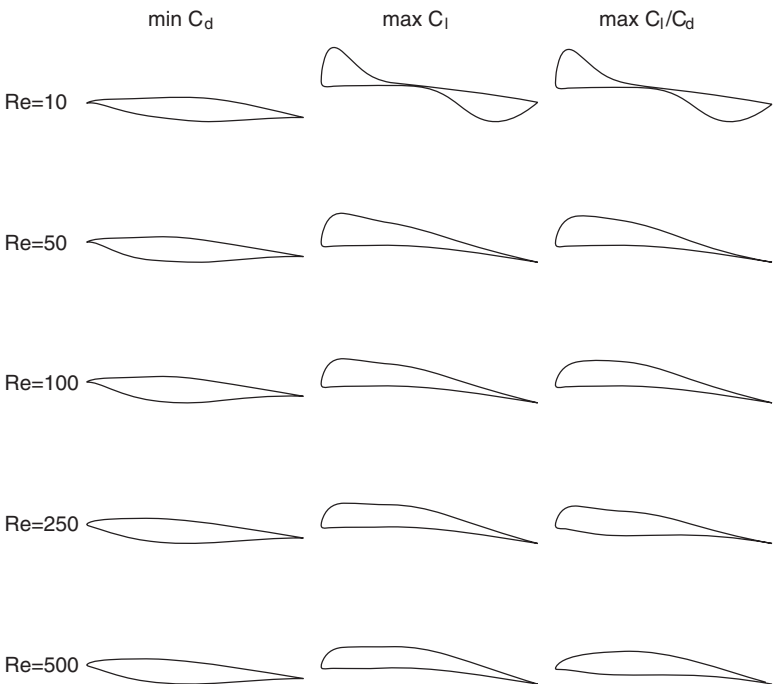

Figure 18. Optimal airfoil shapes obtained with objective functions I_{v1}, I_{v2} and I_{v3} at various Re. The angle of attack is 4°.

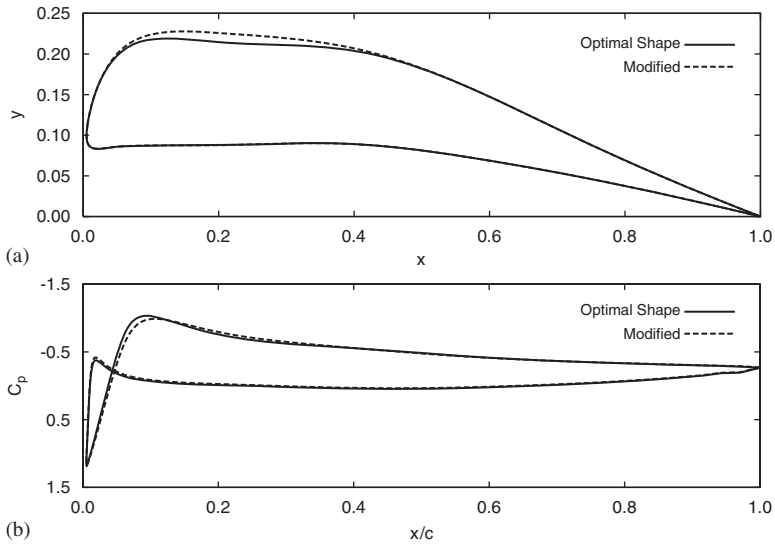

Figure 19. Pressure distribution over the optimal airfoil (I_{v2}) and a modified airfoil at $Re = 250$ along with their shapes.

DOI: 10.1002/fld

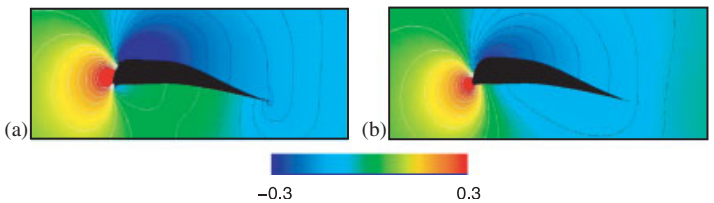

Figure 20. Pressure distribution over (a) optimal airfoil (I_{v2}) and (b) modified airfoil at $Re=250$.

Table V. Drag and lift coefficients of the final shapes at $\alpha=4°$ obtained using various objective functions that include the volume constraint at different Re.

	10		50		100		250		500	
Re	C_d	C_l	C_d	C_l	C_d	C_l	C_d	C_l	C_d	C_l
NACA 0012	1.661	0.238	0.627	0.222	0.423	0.224	0.256	0.224	0.178	0.219
I_{v1}	1.636	0.265	0.619	0.233	0.419	0.229	0.254	0.225	0.176	0.218
I_{v2}	1.911	0.657	0.707	0.517	0.479	0.497	0.300	0.458	0.211	0.426
I_{v3}	1.897	0.645	0.697	0.504	0.474	0.476	0.288	0.405	0.195	0.363

Table VI. The volume enclosed by the final shapes for various objective functions at $\alpha=4°$. The percentage, with respect to V_o, is shown in parentheses.

Re	10	50	100	250	500
V_o	0.08	0.08	0.08	0.08	0.08
I_{v1}	0.0774 (96.75%)	0.0793 (99.125%)	0.0796 (99.5%)	0.0789 (98.625%)	0.0799 (99.875%)
I_{v2}	0.0802 (100.25%)	0.0814 (101.75%)	0.0793 (99.125%)	0.0806 (100.75%)	0.0792 (99.00%)
I_{v3}	0.0799 (99.875%)	0.0800 (100.00%)	0.0802 (100.25%)	0.0792 (99.00%)	0.0782 (97.75%)

pressure field for the two cases is shown in Figure 20. The peak suction on the optimal airfoil is seen to be larger, reflecting the role of dimple.

The third column of Figure 18 shows the final shapes obtained with objective function I_{v3}. Except at $Re=10$, the optimal shapes at other Re appear to be very similar to a conventional airfoil. At $Re=10$, the final shape has high thickness close to the leading and trailing edges. As compared to the NACA 0012 an improvement of 137% in C_l/C_d is seen at $Re=10$, while at $Re=500$ the improvement is 86%. The lift and drag coefficients of the optimal shapes for various objective functions are listed in of Table V. The volume of the optimal shapes along with the percentage deviation from the prescribed volume are listed in Table VI. The maximum deviation is a mere 3%. Almost all the optimal shapes have volume very close to the sought value.

Relative performance of the three objective functions: In general, C_d for the NACA 0012 airfoil appears to be very close to C_d for the optimal shapes obtained with various objective functions as shown in Table V. However, C_l is quite different. Figure 21 shows the variation of the aerodynamic coefficients with Re obtained with various objective functions. Unlike in the earlier cases without the volume constraint, I_{v1} and I_{v2} always leads to the design with lowest C_d and highest C_l, respectively. However, the surprising observation is regarding the maximization of C_l/C_d. I_{v3} fails

DOI: 10.1002/fld

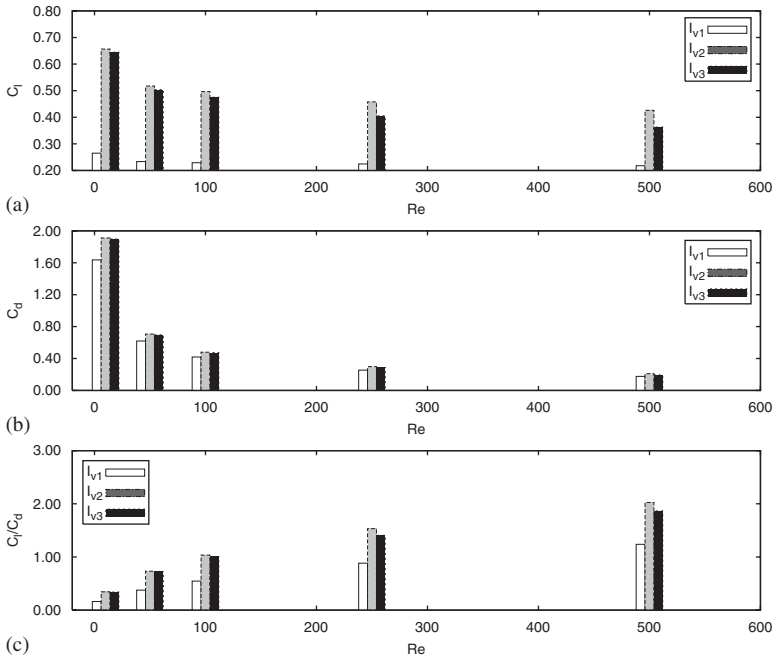

Figure 21. Aerodynamic coefficients of the final shapes obtained from the considered objective function that includes the volume constraint at $\alpha = 4°$: (a) lift coefficient; (b) drag coefficient; and (c) lift to drag ratio.

to outperform the results from I_{v2}. As is seen from Figure 18, the geometries from I_{v2} and I_{v3} are quite similar. However, in general the airfoil shapes in the second column of Figure 18 are more aerodynamically efficient than the ones in the third column. Another interesting effect of the volume constraint is on the trailing edge angle. Most shapes obtained without volume constraint are associated with a trailing edge that is close to a cusp. The volume constraint results in airfoils with finite trailing edge angle.

8.2.2. $\alpha = 12°$. The final shapes obtained with various objective functions are shown in Figure 23. The first column shows the shapes obtained with I_{v1}. The optimal shapes at all Re, except at $Re = 10$, are very similar to the NACA 0012. A reduction of 3% in C_d is seen at $Re = 10$, while at $Re = 500$ the reduction is only 1.5%. The second column of Figure 23 shows the final shapes obtained with objective function I_{v2}. All the optimal shapes have a conventional camber line. Except at $Re = 250$ the final shapes at other Re have a 'tadpole' shape. The final shape at $Re = 250$ appears very similar to the NACA 0012 airfoil. A different initial guess is used to calculate the the optimal solution at $Re = 250$. The optimal solutions obtained with the two initial guesses are shown in Figure 22(a). The second shape produces 0.8% more lift than the first one. In both the cases the design variables do not hit their bounds and, therefore, the gradient of the objective function achieves close to zero value. To check whether both are indeed optimal and stationary values, the variation of the objective function I_{v2} with respect to the design variable 9 (as shown in Figure 2) is computed around the optimal value. The variation is shown in Figure 22(b). It is seen that I_{v2} achieves local

DOI: 10.1002/fld

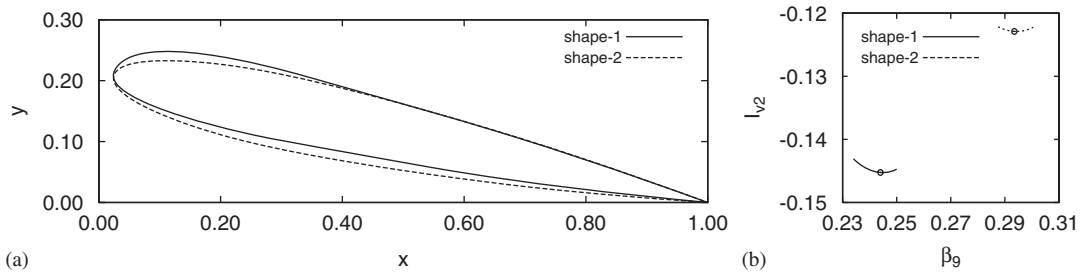

Figure 22. (a) Optimal shapes obtained with two different initial guesses at $Re = 250$ and $\alpha = 12°$ for objective function I_{v2} and (b) variation of the objective function I_{v2} with respect to design variable β_9 for both optimal shapes.

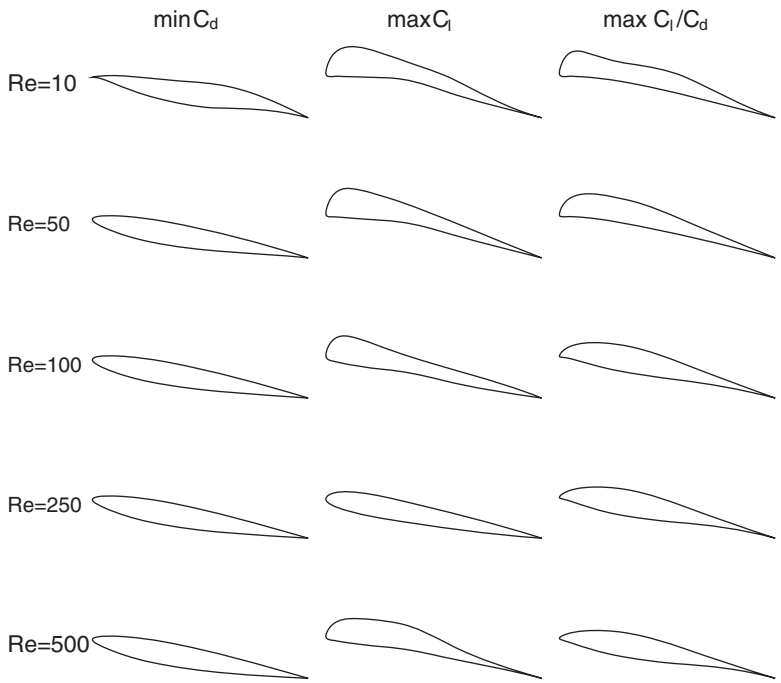

Figure 23. Optimal airfoil shapes obtained with objective functions I_{v1}, I_{v2} and I_{v3} at various Re. The angle of attack is 12°.

minima at both the optimal values. This confirms the oscillatory nature of the objective function with respect to the design variables.

An increase of 42% in C_l is seen at $Re = 10$ while at $Re = 500$ the increase in C_l is 16.5%. The final shapes obtained with objective function I_{v3} are shown in the third column of Figure 23. As in the previous case, optimal shapes at various Re have a conventional camber line. The maximum improvement in C_l/C_d as compared NACA 0012 airfoil is 30% and is obtained at $Re = 10$. The lift and drag coefficients of the optimal shapes are listed in Table VII.

DOI: 10.1002/fld

Table VII. Drag and lift coefficients of the final shapes at $\alpha=12^\circ$ obtained using various objective functions that include the volume constraint at different *Re*.

	10		50		100		250		500	
Re	C_d	C_l	C_d	C_l	C_d	C_l	C_d	C_l	C_d	C_l
NACA 0012	1.728	0.625	0.679	0.594	0.473	0.582	0.302	0.529	0.221	0.449
I_{v1}	1.679	0.625	0.674	0.589	0.468	0.577	0.300	0.526	0.218	0.451
I_{v2}	1.878	0.886	0.784	0.811	0.540	0.665	0.309	0.550	0.267	0.523
I_{v3}	1.846	0.871	0.757	0.802	0.508	0.712	0.321	0.620	0.229	0.559

Relative performance of the three objective functions: Figure 24 shows the variation of the aerodynamic coefficients with *Re* obtained with various objective functions at $\alpha=12^\circ$. For $\alpha=12^\circ$ the NACA 0012 airfoil appears to be very close to optimal for minimum C_d for $Re\geqslant 50$. The effect of α for obtaining optimal performance is clearly seen on comparing Figures 18 and 23. Unlike at $\alpha=4^\circ$, the objective function I_{v3} results in very good designs. For $Re>100$ it outperforms I_{v2} and leads to larger C_l. The C_d obtained is also very comparable to that obtained with I_{v1}.

8.3. *Effect of the number of design variables*

The number of design variables, for a given form of parametrization, plays a crucial role in obtaining an optimal shape. More the design variables, the richer is the design space. One possibility is to use the surface coordinates themselves as design variables [8]. However this can make the computations very expensive and may also lead to non smooth surfaces. To study the effect of the number of design variables, three different parametrization of the NACA 0012 are used to obtain an optimal surface. The objective is to obtain an optimal surface having the largest lift coefficient at $\alpha=4^\circ$ and $Re=250$. The three parametrization have 13, 19 and 27 control points, respectively. The control polygon along with the control points of the three parametrization are shown in the first column of Figure 25. The second column of Figure 25 shows the surfaces that result from the optimization. The optimal shape obtained with 13 control points leads to a conventional airfoil while the other two parametrization lead to shapes whose trailing edge thickness progressively increases. The lift coefficient also increases with increase in the number of control points. In any situation the number of design variables one can use is limited by available resources and other constraints such as the simplicity of optimal geometry. This study shows the relevance of the number of design variables in shape optimization.

9. CONCLUSIONS

A continuous adjoint approach for shape optimization of airfoils in steady low Reynolds number flows has been implemented. A stabilized finite element method based on SUPG/PSPG stabilization has been used to solve, both, the flow and adjoint equations. The airfoil shape is represented by a NURBS curve. The y-coordinates of the control points have been used as design variables.

Flow over a NACA 0012 airfoil is studied at $Re\leqslant 500$. Flow is seen to be sensitive to, both, *Re* and α. For low α, the slope of $C_l-\alpha$ curve is seen to be linear. Nonlinear behavior is observed for $\alpha>6^\circ$. Unlike the stall behavior observed at higher *Re*, the $C_l-\alpha$ variation remains monotonic for

DOI: 10.1002/fld

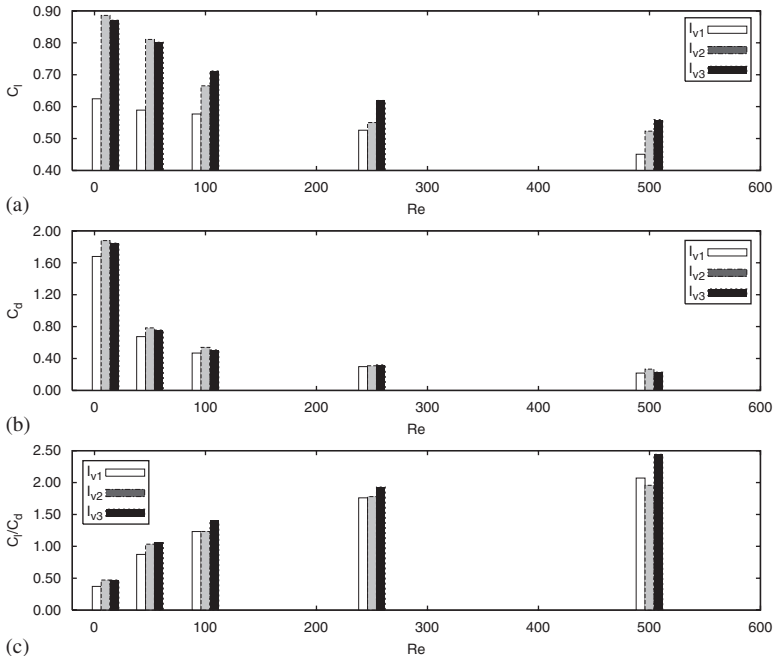

Figure 24. Aerodynamic coefficients of the final shapes obtained from the considered objective function that include the volume constraint at $\alpha = 12°$: (a) lift coefficient; (b) drag coefficient; and (c) lift to drag ratio.

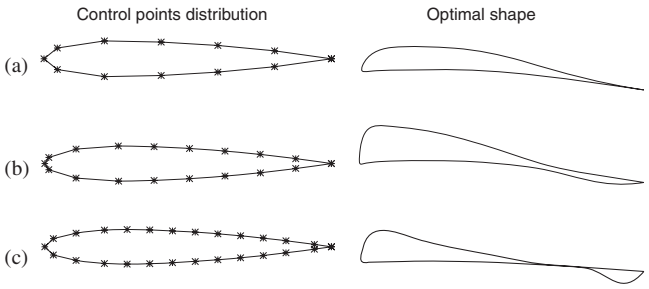

Figure 25. $\alpha = 4°$, $Re = 250$ flow past an airfoil: The distribution of the control points is shown on left and the optimal geometry obtained is shown on the right for (a) 13; (b) 19; and (c) 27 control points.

$Re \leqslant 500$. The effect of Re is investigated in detail for $\alpha = 4°$ and 12°. At $\alpha = 4°$, C_l shows a non-monotonic variation with Re at $Re \sim 50$. This is caused by the fact that the pressure contribution to C_l decreases while the viscous contribution increases with increase in Re. At $\alpha = 12°$, C_l decreases quite significantly with increase in Re. C_d is found to decrease with increase in Re for, both, $\alpha = 4°$ and 12°.

Five different objective functions are evaluated to obtain an optimal airfoil. They are (1) minimize drag (I_1), (2) maximize lift (I_2), (3) maximize lift to drag ratio (I_3), (4) maximize lift and minimize drag (I_4) and (5) minimize drag coefficient at constant lift (I_5). Optimal shapes are obtained for

DOI: 10.1002/fld

$Re \leqslant 500$ at $\alpha = 4°$ and 12°. Airfoils with least C_d are produced by shapes arising from the objective function I_1. However, it is seen that shape with largest C_l does not always result from objective function I_2. I_3 produces the shapes with the largest C_l/C_d. I_4 is seen to be biased towards the larger contributor to the objective function. At low *Re*, when C_d is the larger contributor, the shapes obtained are similar to the ones obtained from I_1. At high *Re*, the optimal shapes resemble the ones obtained from I_2 since the larger contributor to I_4 is C_l. I_5 is also seen to be dependent on the larger contributor amongst the two terms to the objective function.

A volume constraint is added to the objective functions (I_{v1}, I_{v2}, I_{v3}) and the study is repeated. Again, the shapes with the least C_d are obtained from the objective function I_{v1}. As is the case without volume constraint, no objective function shows a clear preference while maximizing the lift coefficient. This study demonstrates the necessity to consider several objective function to reach an optimal design while using an algorithm that seeks local optima. It is shown that the objective functions have an oscillatory nature with respect to the design variable and, therefore, have multiple local optima. The optimizer, depending on the initial guess, reaches the closest local optima. The effect of the number of control points on the optimization process is studied. Three different parametrization having 13, 19 and 27 NURBS control points are used. It is seen that with more design variables, the design space gets richer and the optimizer is able to determine a better solution. But this comes at the expense of increased computation.

This study clearly brings out the need to create a database for high performance airfoils for low *Re* applications. In this work a optimization study has been carried out for two values of α and different shapes have been obtained. It is worthwhile to extend the study to find an optimal shape that gives good performance for a range of α. The work is also being extended to find optimal geometries for unsteady flows.

REFERENCES

1. Obayashi S, Takanashi S. Genetic optimization of target pressure distributions for inverse design methods. *AIAA Journal* 1996; **34**(5):881–886.
2. Burg COE, Newman JC III. Computationally efficient, numerically exact design derivatives via the complex Taylor series expansion method. *Computers and Fluids* 2003; **32**:373–383.
3. Sherman LL, Taylor VC III, Green LL, Newman PA, Hou GJW, Korivi M. First and second order aerodynamic sensitivity derivatives via automatic differentiation with incremental iterative methods. *Journal of Computational Physics* 1994; **129**:307–331.
4. Hou GJW, Sheen JS, Chuang CH. Shape sensitivity analysis and design optimization of linear thermoelastic solids. *AIAA Journal* 1992; **30**:528–537.
5. Giles MB, Pierce NA. An introduction to the adjoint approach to design. *Flow, Turbulence and Combustion* 2000; **65**:393–415.
6. Pironneau O. On optimum profiles in Stokes flow. *Journal of Fluid Mechanics* 1973; **59**:117–128.
7. Pironneau O. On optimum design in fluid mechanics. *Journal of Fluid Mechanics* 1974; **64**:97–110.
8. Jameson A. Aerodynamic design via control theory. *Journal of Scientific Computing* 1988; **59**:117–128.
9. Nadarajah S, Jameson A. Studies of the continuous and discrete adjoint approaches to automatic aerodynamic optimization. *AIAA Paper 2000-0667*, 2000.
10. Abraham FV. Stabilized finite element solution of optimal control problems in computational fluid dynamics. *Ph.D. Dissertation*, Mechanical Engineering and Materials Science, Rice University, 2004.
11. Srinath DN, Mittal S. A stabilized finite element method for shape optimization in low Reynolds number flows. *International Journal for Numerical Methods in Fluids* 2007; **54**:1451–1471.
12. Mueller TJ. Fixed and flapping wing aerodynamics for micro air vehicle applications. *AIAA Progress in Astronautics and Aeronautics*, 2001.
13. Ho CM, Tai YC. Micro-electro-mechanical-systems (MEMS) and fluid flows. *Annual Review of Fluid Mechanics* 1998; **30**:579–612.

DOI: 10.1002/fld

14. Epstein AH, Senturia SD, Anathasuresh G, Breuer K, Chen KS, Ehrich FE, Gauba G, Ghodssi R, Groshenry C, Jacobson S, Land JH, Lin CC, Mehra A, Miranda JM, Nagle S, Orr DJ, Piekos E, Schmidt MA, Shirley G, Spearing MS, Tan CS, Tzeng YS, Waitz IA. Power MEMS and microengines. *Transducers '97*, *The 9th International Conference on Solid-state Sensors and Actuators*, 1997.
15. Bardina J, Rajkumar T. Micro-flying robotics in space missions. *SAE Transactions* 2005; **114**:1368–1374.
16. Jacobs EN, Sherman A. Airfoil section characteristics as affected by variations of the Reynolds number. *NACA-TR-586*, 1937.
17. Aerodynamic characteristics of airfoils. *NACA-TR-93*, 1921.
18. Anderson W, Bonhaus D. Airfoil design on unstructured grids for turbulent flows. *AIAA Journal* 1999; **36**:185–191.
19. Brezillon J, Gauger NR. 2D and 3D aerodynamic shape optimization using the adjoint approach. *Aerospace Science and Technology* 2004; **8**:715–727.
20. Carmichael BH. Low Reynolds number airfoil theory. *NASA-CR-165803-VOL-1*, vol. 1, 1981.
21. Thom A, Swart P. The forces on an aerofoil at very low speeds. *Journal of the Royal Aeronautical Society* 1940; **44**:761–770.
22. Sunada S, Sakaguchi A, Kawachi K. Airfoil section characteristics at low Reynolds numbers. *Journal of Fluids Engineering* 1997; **119**:129–135.
23. Sun Q, Boyd ID. Flat-plate aerodynamics at very low Reynolds numbers. *Journal of Fluid Mechanics* 2004; **502**:199–206.
24. Kunz PJ. Aerodynamics and design for ultra-low Reynolds number flight. *Ph.D. Dissertation*, Stanford University, 2003.
25. Yahi H, Kawahara M. Optimal shape determination of a body located in incompressible viscous fluid flow. *Computer Methods in Applied Mechanics and Engineering* 2007; **196**:5084–5091.
26. Tezduyar TE, Behr M, Mittal S, Johnson AA. Computation of unsteady incompressible flows with the finite element methods–space-time formulations, iterative strategies and massively parallel implementations. In *New Methods in Transient Analysis*, Smolinski P, Liu WK, Hulbert G, Tamma K (eds). ASME: New York, 1992; **143**:7–24.
27. Tezduyar TE, Mittal S, Ray SE, Shih R. Incompressible flow computations with stabilized bilinear and linear equal order interpolation velocity pressure elements. *Computer Methods in Applied Mechanics and Engineering* 1992; **95**:221–242.
28. Byrd RH, Lu P, Nocedal J, Zhu C. A limited memory algorithm for bound constrained optimization. *SIAM Journal on Scientific Computing* 1995; **16**:1190–1208.
29. Gerald F. *Curves and Surfaces for Computer Aided Geometric Design. A Practical Guide*. Academic Press: San Diego, U.S.A., 1990.

DOI: 10.1002/fld